Journal of Power Sources 194 (2009) 950–960

Contents lists available at ScienceDirect

Journal of Power Sources

journal homepage: www.elsevier.com/locate/jpowsour

# Microcracking in electron beam deposited scandia-stabilised zirconia electrolyte

Mykola Lugovy[a,*], Viktor Slyunyayev[a], Robert Steinberger-Wilckens[b]

[a] Institute for Problems of Materials Science, 3 Krzhizhanovskii Str, 03142 Kiev, Ukraine
[b] Forschungszentrum Jüelich, Jüelich, Germany

ARTICLE INFO

*Article history:*
Received 22 February 2009
Received in revised form 30 April 2009
Accepted 15 May 2009
Available online 22 May 2009

*Keywords:*
Microcracking
Residual stress
Scandia-stabilised zirconia
Electrolyte
Thermal expansion
Solid oxide fuel cell

ABSTRACT

It is the aim of the present work to address some of the aspects of microcracking in electron beam deposited scandia-stabilised zirconia electrolyte applied for solid oxide fuel cells (SOFC) where a thin electrolyte layer is deposited on a relatively thick anode substrate. A model of microcracking for the electrolyte material is proposed which takes into account the statistical distribution of grain sizes, the stress redistribution due to failure of individual structural elements as well as the local criterion of grain fracture. The combination of electron microscopy research with model calculations permits both the specific energy of new surface creation in the electrolyte and critical parameters of the microcracking process to be determined. The annealing-induced electrolyte microcracking discussed in this work corresponds to localised microcracking, where each next structural element fails mainly at an existing microcrack tip. The features of localised microcracking in electron beam deposited scandia-stabilised zirconia electrolyte are analysed.



## 1. Introduction

Solid oxide fuel cells (SOFC) offer promising options for future energy supply due to the high electrical energy conversion efficiency they display (up to 60%). SOFC have a particularly wide range of applications ranging from centralised MW scale generation through to localised applications at 100+ kW level for distributed generation to local domestic generation on the 1–10 kW scale [1] and as Auxiliary Power Units on board of vehicles (automotive, maritime and aerospace). There is also a wide range of other applications where cleaner energy is required, such as corrosion protection, uninterruptible power supply, remote generation, and domestic appliances. Another recent fuel cell development is the miniaturised "palm-power" units of 100 mW–10 W for portable electronic devices. Commercialisation of these applications will require even lower operating temperatures and additional material improvements [2].

A single SOFC consists of an air electrode (cathode), electrolyte, and a fuel electrode (anode) [3]. The electrolyte's function is to allow the transport of oxide ions from the electrolyte's interface with the air electrode to its interface with the fuel electrode. The function of the air electrode is to facilitate the reduction of oxygen molecules to oxide ions transporting electrons to the electrode/electrolyte interface and allowing gas diffusion to and from this interface. The function of the fuel electrode is to facilitate the oxidation of the fuel and the transport of electrons from the electrolyte to the fuel electrode interface. In addition it must allow diffusion of fuel gas to and exhaust gases away from this interface.

Still, several major development problems remain: degradation is too high (between 0.5 and 2% per 1000 h of operation, resulting in a 'lifetime' of around 10,000–30,000 operating hours) [4]; costs are too high (above 10,000€/kW); intermittent operation (thermal and oxidation cycling) results in increased degradation and/or failure; power density at temperatures below 1023 K is comparatively low [5]. These problems are a consequence of the high temperatures, elevated pressures required for their operation, and the ceramics materials properties [6].

The use of electrolytes with higher ion conductivity, for instance scandia-stabilised zirconia (ScSZ), offers the potential for lowering the operating temperature with an ensuing reduction of corrosion and degradation effects. SOFC operating between 873 and 1073 K are generally labelled "intermediate temperature" SOFC (IT-SOFC). On the other hand, the higher conductivity can also be read as a potential for obtaining very much higher power densities at operating temperatures above 1023 K. I.e., these materials do not only offer an improvement in lifetime of SOFC, they could also be used to increase the compactness of Auxiliary Power Units on board of vehicles under volume and weight constraints. Another way of minimising ohmic losses across the electrolyte is to use thin electrolyte membranes with thicknesses between 5 and 50 μm. Electron beam deposition (EBD) is a promising technique to produce thin films of electrolyte on thick anode substrates of planar geometry. The anode supported planar SOFC cell has become one of the most widespread SOFC types.

* Corresponding author. Tel.: +380 444242524; fax: +380 444242131.
*E-mail address:* nil2903@gmail.com (M. Lugovy).

0378-7753/$ – see front matter © 2009 Elsevier B.V. All rights reserved.
doi:10.1016/j.jpowsour.2009.05.024

A challenge with the planar geometries is in obtaining mechanically stable structures, as thin layer ceramics are inherently susceptible to failure when subjected to moderate stress. If the anode is produced from a nickel oxide–ScSZ composite and the electrolyte from scandia-stabilised zirconia, thermal mismatch stresses keep the electrolyte layer under compression at room temperature and under tension at temperatures higher than the deposition temperature.

The mechanical properties of the SOFC components, including the electrolyte, must be known in order to design an optimal SOFC structure. Typically, the electrolyte shows microcracking due to residual stress [7–9]. Electrolytes deposited by electron beam technique are thin films with specific columnar structure attached to a weak anode layer. It is impossible, though, to obtain bulk specimen for mechanical testing with a microstructure which is identical to the electron beam deposited electrolyte. Furthermore, indentation methods are unable to determine the in-plane electrolyte mechanical properties. Firstly, unknown residual stresses due to edge effects change the indentation response [10]; secondly, the columnar microstructure and average grain size comparable with the film thickness do not allow imprints which contain enough grains (at least 10) for the necessary averaging of properties. In such a way, the determination of the mechanical properties of electron beam deposited electrolytes is complicated scientific problem.

One possible approach to solve the problem of description and prediction of the mechanical behaviour of such objects is microcracking modelling. Generalising existing structural models of mechanical behaviour of materials with microcracks [11–18], it should be noted, that all of them contain the following issues: structural element (SE) identification; local failure criterion for SE; stress redistribution due to material damage; total failure criterion.

It is the aim of the present work to address some of the aspects of microcracking in electron beam deposited scandia-stabilised zirconia electrolytes applied on a fuel cell anode. In order to gain better insight into the mechanical behaviour of the electrolyte, the structural model of scattered microcracking in thin brittle films was developed. The work focuses on the determination of both the specific energy of new surface creation within the electrolyte and critical parameters of microcracking processes using the combination of electron microscopy research of annealed and as-deposited electrolyte with model calculations.

## 2. Experimental

The composition 10 mol.% $Sc_2O_3$–1 mol.% $CeO_2$–89 mol.% $ZrO_2$ (10Sc1CeSZ) was found to be optimal for the electrolyte and as a constituent of the anode [19,20]. Powders manufactured at the Institute for Problems of Materials Science were used for half-cell production due to the greater sintering ability and electric conductivity compared with powders from other manufacturers.

SOFC anodes were fabricated with a traditional ceramic route [19]. Mixtures of 40 wt.% NiO and 60 wt.% 10Sc1CeSZ were ball-milled with alcohol for 24 h. Polyvinyl alcohol was used as pore-creating agent. Specimens were made by uniaxial pressing using pressure ~20 MPa. These were sintered at 1723 K for 2 h in air. The anode substrates were found to meet all necessary requirements concerning both strength and porosity (100–150 MPa and 25–30%, respectively). The thickness of the anodes was 990 μm.

Electron beam deposition (EBD) technique was used for producing electrolyte films deposited on the porous, non-reduced anode substrates. Hereafter the electrolyte–anode layered system will be termed "half-cell".

EBD is one form of physical vapor deposition (PVD). An electron beam is directed at a target pellet, in order to ionize and melt the target material, which is then accelerated in an electrical field and deposits on the specimen to be coated. The process is rather slow but results in a very precise control of layer thickness and, when applied expertly, delivers very thin, dense coatings, as needed for intermediate temperature electrolytes [21]. These thin layers again reduce the overall resistance of the electrolyte and further support the trend towards higher power density/lower operating temperatures. Powder metallurgy routes were applied to produce ScSZ specimens to be used for further electron beam deposition experiments. The dimensions of the cylindrically shaped specimens were about 4 mm in diameter and about 8 mm in height (porosity approx. 15%). The substrates were subjected to temperatures of 873, 1023, and 1173 K (deposition temperature) during the deposition process. The deposition time of 15 min resulted in the formation of electrolyte films with 10 μm in thickness.

To obtain a mechanical loading of the electrolyte, half-cells were annealed at 1173, 1178, 1473, 1548 and 1633 K for 2 h. Heating the electrolyte to a temperature higher than the deposition temperature induces equibiaxial tension due to a thermal expansion mismatch between electrolyte and anode layers. The thermal stresses in half-cells during annealing can be calculated from layer properties and the difference between annealing and deposition temperatures using the method presented in [22,23]. The layer properties required for the model calculations are elastic moduli, Poisson ratios, coefficients of thermal expansion (CTE), and layer thicknesses.

Standard techniques, scanning electron microscopy and Image-Pro Plus Software (Version 3.0.00.00, "Media Cybernetics"), were applied to obtain electrolyte microstructure images and to evaluate the statistical distribution of grain and microcrack sizes as well as the number of microcracks, average microcrack size and the standard deviation in the electrolyte layer. Using Image-Pro Plus Software for all considered states of electrolyte, the length of each microcrack observed in corresponding image was measured. The microcrack density was calculated as

$$f_f = \frac{1}{A}\sum_{i=1}^{N_A} c_i^2, \tag{1}$$

where $c_i$ is the effective length of the $i$th microcrack, and $N_A$ is the number of microcracks on the scanned area $A$ (in our case $A = 45{,}000\ \mu m^2$). The number of microcracks per one grain $n^*/n_g^*$ can be determined from

$$\frac{n^*}{n_g^*} = \frac{N_A}{N_g}, \tag{2}$$

where $n^*$ is the number of cracks per area unit, $n_g^*$ is the number of grains per area unit, and $N_g$ is the number of grains on the scanned area $A$.

Thermal expansion analysis of anode material specimens (of size 4 mm × 4 mm × 20 mm) was performed to obtain information about the coefficients of thermal expansion. The data were measured with a highly sensitive quartz dilatometer having the optical system for specimen length measurement. Due to optical magnification within the range 4000× to 10,000× the usage of such a technique allows the measurement accuracy of specimen length to reach 0.00025–0.0001 mm. CTE measurements were made in air in the wide temperature range of 293–1223 K. The heating and cooling rates were 10 and 20 K $min^{-1}$, respectively. The quartz thermal expansion was accounted for in the SOFC constituent CTE measurements. The CTE was calculated from the expression

$$\alpha_{t_1-t_2} = \frac{r(A_2 - A_1)}{Rl(t_2 - t_1)} + \alpha_q, \tag{3}$$

where $l$ is the specimen length; $r$ is the roller radius; $A_1$ and $A_2$ are the specimen length values corresponding to temperatures $t_1$ and $t_2$, respectively; $R = 1000$ mm is the roller-scale distance; $\alpha_q$ is the CTE of quartz.

The elastic modulus of the anode material was determined by using four-point bending tests with an Instron testing machine (internal and external spans were 20 and 40 mm, respectively). Specimens of 4 mm × 5 mm × 45 mm in size were used for the tests.

Disc-shaped samples of anode substrates and half-cells were loaded in biaxial ring-on-ring bending tests. The test conditions followed the procedures recommended in the ASTM standard C 1499-05 [24]. The data were evaluated using the equations for linear bending theory. Accordingly, the equibiaxial flexure stress was derived from:

$$\sigma = \frac{3P}{2\pi t^2}\left[(1+\nu)\ln\left(\frac{r_2}{r_1}\right) + \frac{1-\nu}{2}\left(\frac{r_2^2 - r_1^2}{r_3^2}\right)\right], \quad (4)$$

where $P$ is the applied force, $t$ is the specimen thickness, $\nu$ the Poisson ratio and $r_1$, $r_2$ and $r_3$ are the radii of the load ring, supporting ring and (circular) specimen, respectively. The values of $t$, $r_1$, $r_2$ and $r_3$ were 1, 9, 18.6 and 23.8 mm, respectively. Since the number of tests was limited (five tests for anode substrates and five tests for half-cells), only the mean value and the standard deviation are given. Equibiaxial flexure tests were carried out up to failure at room temperature (RT) in air. The loading rate was 100 N min$^{-1}$ in all tests.

## 3. Model

The structural element of the electrolyte in the model is the individual grain, intact or cracked. The characteristics of the individual structural elements have some statistical scatter and the loading parameters determine the number of cracked elements. Each structural element is considered as located in effective media. The minimal size of a cracked grain and the failure probability can be found using local failure criteria. The failure probability of an individual structural element will determine the relative number of failed elements.

For a single-phase electrolyte the main parameter in determining the stress redistribution is its elastic modulus $E$. The main loading parameter in the model is the strain energy density:

$$q = \frac{\sigma^2}{2E}, \quad (5)$$

where $E = E(e)$, i.e. the elastic modulus is a function of strain $e$. Additionally, the elastic modulus of an undamaged electrolyte $E_0$ also affects the stress redistribution. The strength of an individual element depends on the specific energy of the new surface creation, $\gamma$. This energy is the surface energy of the material in the simplest case of uniaxial tension and transcrystalline fracture.

The statistical distribution of the structural element sizes is determined by few factors depending on the material fabrication technology. Typically, a logarithmic normal distribution of grain sizes is used [11,12,15,16]. Its density can be expressed as:

$$f(l) = \frac{1}{lD\sqrt{2\pi}}\exp\left(-\frac{(\ln\, l - M)^2}{2D^2}\right), \quad (6)$$

where $l$ is the grain size; $M$ is the mathematical expectation of $\ln l$; $D^2$ is the dispersion of the distribution.

It should be noted that real specimen contains finite numbers of grains. Therefore, if grain sizes obey the logarithmic normal distribution, grains with size larger than a certain size $l_{max}$ cannot be observed. The number of grains larger than $l_{max}$ can be determined as $N_s p$, where $N_s$ is the total number of grains in the specimen, $p$ is the probability of existence of a grain with size larger than $l_{max}$ in the specimen:

$$p = \int_{l_{max}}^{\infty} f(l)\ dl. \quad (7)$$

From a physical point of view, the size $l_{max}$ can be defined as that size for which the total number of grains with size larger than $l_{max}$ equals 1. In fact, this results in absence of such grains in the specimen. In such a way, $l_{max}$ can be determined from the following equation for a given logarithmic normal distribution:

$$N_s \int_{l_{max}}^{\infty} f(l)\ dl = 1. \quad (8)$$

A strain energy density criterion is used as the local failure criterion in the model. The failure criterion is based on an energetic approximation of crack nucleation conditions [25]. It allows to solve the problem of a random flaw in a grain postulating the existence of a single critical defect with a size proportional to the grain size. The local failure criterion based on the strain energy density can be expressed as $\beta q > q_c$, where $q_c$ is the critical value of the strain energy density which is a function of grain size. The coefficient $\beta$ characterises the strain energy density and stress redistribution between undamaged material and the effective continuum consisting of undamaged and cracked structural elements. According to [26], $\beta$ is considered to be approximated by the ratio of elastic moduli of undamaged and damaged materials, i.e. in our case $\beta = E_0/E$.

The parameter $q_c$ for brittle material can be determined from energy balance condition as follows:

$$q_c = \frac{K\gamma}{l}, \quad (9)$$

where $K$ is the geometrical factor of the structural element. In many important applications of microcracking models we have a so-called 2D case when a thin layer of material contains microcracks through the full thickness [27,28]. More specifically, a thin layer can be defined as the layer with thickness less than one or two average grain sizes. In this case, for an in-plane isotropic layer in first approximation, the individual grains can be considered as circular cylinders with height equals to the layer thickness. Then, from the ratio of crack surface area and structural element volume the geometrical factor equals $8/\pi$ for transcrystalline cracks when a crack is located along the diameter of a cylinder. This factor is 8 for intercrystalline cracks when the crack coincides with the lateral surface of a cylinder.

The dependencies of elastic modulus and Poisson ratio on the damage parameter (hereinafter referred to as microcrack density) for the 2D case presented in [27] are:

$$\frac{E}{E_0} = \exp\left(\frac{-\pi f_f}{4}\right), \quad (10)$$

$$\frac{\nu}{\nu_0} = \exp\left(\frac{-\pi f_f}{4}\right), \quad (11)$$

where $f_f = n^*\langle c^2\rangle$ is the microcrack density, $c$ is the crack length, angular parentheses denote averaging over all cracks, $\nu_0$ is the Poisson ratio of undamaged material.

The minimal size of a failed grain $l^*$ can be determined from the equation

$$\beta q = q_c \quad (12)$$

and Eq. (9) for $l = l^*$. In the framework of our failure criterion, all grains with size larger than $l^*$ will be cracked and grains with size less than $l^*$ remain undamaged. Note that $l^*$ depends on microcrack density in material through $\beta$.

The normalised strain energy density is defined as

$$q^* = q\frac{l_m}{\gamma}, \quad (13)$$

where $l_m$ is the average grain size. The normalised stress and strain are $\sigma^* = \sigma\sqrt{l_m/E_0\gamma}$ and $e^* = e\sqrt{E_0 l_m/\gamma}$, respectively.

In the 2D case the microcrack density of the damaged layer can be determined as:

$$f_f = n^* \int c^2 f_c(c)\ dc, \tag{14}$$

where $\langle c^2 \rangle = \int c^2 f_c(c)\,dc$, $f_c(c)$ is the density of the statistical distribution of microcrack sizes. Under the condition that each microcrack occupies only a single grain (so-called scattered microcracking) and the microcrack size equals the grain size, the density of the microcrack size distribution for grains with size larger than $l^*$ can be found from the grain size distribution:

$$f_c(c) = \frac{f(c)}{\int_{l^*}^{l_{\max}} f(l)\ dl}. \tag{15}$$

The denominator in (15) supplies the normalisation of the distribution density function. Note that $f_c(c) = 0$ for cracks with size less than $l^*$ and grains with size larger than $l_{\max}$ are not considered. The fraction of failed grains (microcrack number per grain) is

$$\frac{n^*}{n_g^*} = \int_{l^*}^{l_{\max}} f(l)\ dl. \tag{16}$$

Note that

$$\frac{1}{n_g^*} = \frac{\pi}{4} \int_0^{l_{\max}} l^2 f(l)\ dl \tag{17}$$

is the average area of a single grain, if we consider grains as circular cylinders for simplification.

The main model equations for scattered microcracking of a single-phase thin layer of brittle material taking into account (9), (10), (12), (15), (16) are:

$$f_f = \frac{4}{\pi} \frac{\int_{l^*}^{l_{\max}} l^2 f(l)\ dl}{\int_0^{l_{\max}} l^2 f(l)\,dl}, \tag{18}$$

$$l^* = \frac{2K\gamma E_0}{\sigma^2 \exp(\pi f_f/2)}, \tag{19}$$

$$\langle c \rangle = \frac{\int_{l^*}^{l_{\max}} l f(l)\,dl}{\int_{l^*}^{l_{\max}} f(l)\,dl}, \tag{20}$$

$$s^2 = \frac{\int_{l^*}^{l_{\max}} l^2 f(l)\,dl}{\int_{l^*}^{l_{\max}} f(l)\,dl} - \langle c \rangle^2, \tag{21}$$

where $\sigma$ is the stress acting in the electrolyte; $\langle c \rangle$ is the average microcrack size; and $s$ is the standard deviation of microcrack size. Using substitution of (19) to (18), the dependence $\sigma$ on $f_f$ can be calculated. Taking into account

$$q = \frac{\sigma^2}{2E} = \frac{\sigma^2}{2E_0} \exp\left(\frac{\pi f_f}{4}\right), \tag{22}$$

the dependence of strain energy density on microcrack density can be determined as well.

## 4. Results and discussion

The electrolyte layer in an IT-SOFC is a single-phase anisotropic material with the anisotropy resulting from its processing route. The thin layer of electrolyte has a columnar structure where grains are orientated perpendicular to the specimen surface (Fig. 1a). Nevertheless, such a structure is isotropic in the plane of the electrolyte, i.e. the properties of the film in different directions within the plane are identical. The main structural elements of the electrolyte which are subject to microcracking are its grains. The electrolyte microcracking is in fact a 2D case because all cracks formed in the electrolyte layer are oriented perpendicular to its plane. According to SEM investigations the intercrystalline fracture mode is revealed (Fig. 1a).

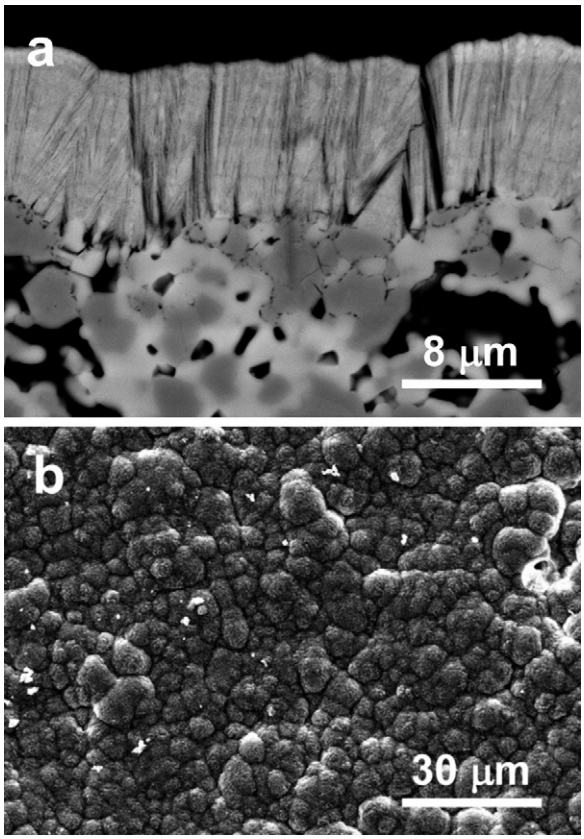


**Fig. 1.** Microstructure of as-deposited EBD 10Sc1CeSZ electrolyte film (deposition temperature 1173 K): (a) side view (intercrystalline fracture and columnar structure of electrolyte) and (b) top view.

The microstructure of the as-deposited electrolyte film (deposition temperature 1173 K) is shown in Fig. 1b, where the boundaries between the structural elements are distinctly visible. It was found experimentally that the distribution of grain sizes in the electrolyte demonstrates a slight dependence on deposition temperature. Therefore, in first approximation, it is reasonable to use a common distribution which is the same for all deposition temperatures in the model. The distribution of grain sizes in the electrolyte is shown in Fig. 2a, the distribution of normalised grain sizes is shown in Fig. 2b. According to experimental data, the average grain size in the electrolyte is 6.64 μm, the standard deviation is 1.53 μm. It was found also, that the experimental statistic distribution of normalised grain sizes can be approximated with sufficient accuracy by a logarithmic normal distribution (Fig. 2b) with parameters $M = -0.02601$, $D^2 = 0.052028$, $l_{\max} = 17$ μm.

One of the possible approaches to characterise the mechanical properties of EBD electrolyte films is to use heat treatment, i.e. annealing at various temperatures above deposition temperature followed by electron microscopy investigation of the electrolyte surface. The annealing creates equibiaxial stress states with tensile stress in the electrolyte, whose value depends on the difference $\Delta T$ between annealing temperature and deposition temperature. Electron microscopy investigations of the electrolyte surface have allowed the density of microcracks arising due to tensile residual stresses in the annealed electrolyte to be determined (Fig. 3).

The initial data for thermal stress calculation in half-cells were established experimentally and via literature survey. The elastic modulus for the anode material was found to be 81 GPa from four-point bending tests. The elastic modulus of an undamaged

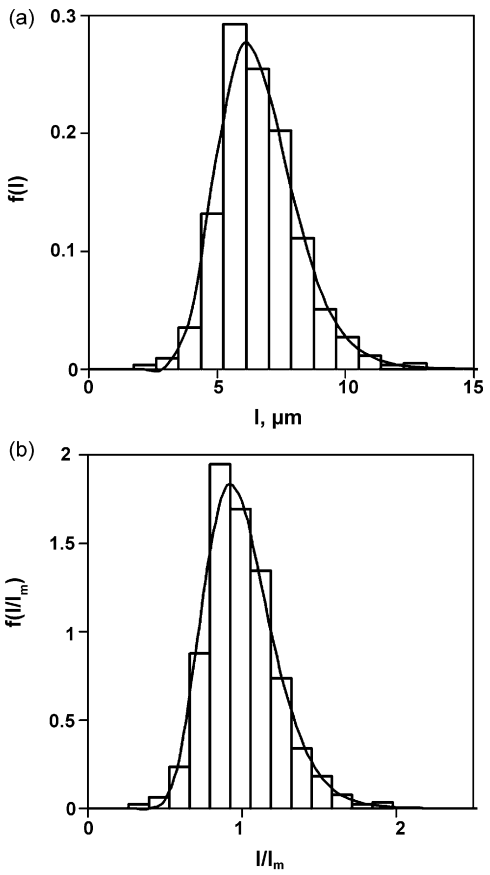


**Fig. 2.** Statistical distribution of structural element sizes in as-deposited EBD 10Sc1CeSZ electrolyte film: (a) non-normalised and (b) normalised; the curves indicate the corresponding logarithmic normal distributions.

electrolyte was adopted to be 200 GPa [29]. It is known that the elastic modulus of ceramics as a rule demonstrates a dependence on temperature. For example, the existence of such dependence for yttria-stabilised zirconia (YSZ) is shown in [30] where a substantial scattering of experimental data is observed. The scattering complicates the determination of a reliable dependence of elastic modulus on temperature. To the best of our knowledge, the temperature dependence of the elastic modulus for 10Sc1CeSZ is not available from literature. Therefore, as a first approximation, a constant value of the elastic modulus is used for calculation in this work. The Poisson ratios of anode and electrolyte were adopted to be 0.3 and 0.31, respectively [30]. The coefficient of thermal expansion for the anode was found experimentally to be $11.7 \times 10^{-6}\,K^{-1}$. The coefficient of thermal expansion for the electrolyte was adopted to be $1 \times 10^{-5}\,K^{-1}$ [31]. Note that non-reduced anode substrate was used in this work. In such a way, there are no particles of pure nickel in the anode. This means that creep processes in the anode during annealing were negligible, simplifying residual stress calculation.

The validity of the initial data and thermal stress calculation procedures in half-cell specimen is confirmed by results of ring-on-ring mechanical tests. The fracture stress of anode specimens is found to be $41.5 \pm 4.0$ MPa. The fracture stress of half-cell specimens corresponding to anode failure is $28.1 \pm 3.0$ MPa. The resulting decrease of anode strength (13.4 MPa on the average) is associated with residual tensile stresses in the anode near the anode/electrolyte interface. The calculated value of residual stress in the anode is 16 MPa (tension) which is in good accord with the anode strength decrease, confirming hereby the validity of the residual stress calculation.

It is found that the microcrack density is negligible at $\Delta T = 150$ K demonstrating the practical absence of microcracking due to stresses associated with this temperature difference. Increasing the temperature difference gives rise to a growth of the microcrack density which promotes the significant decrease of the electrolyte elastic modulus and Poisson ratio [27]. In turn, this results in

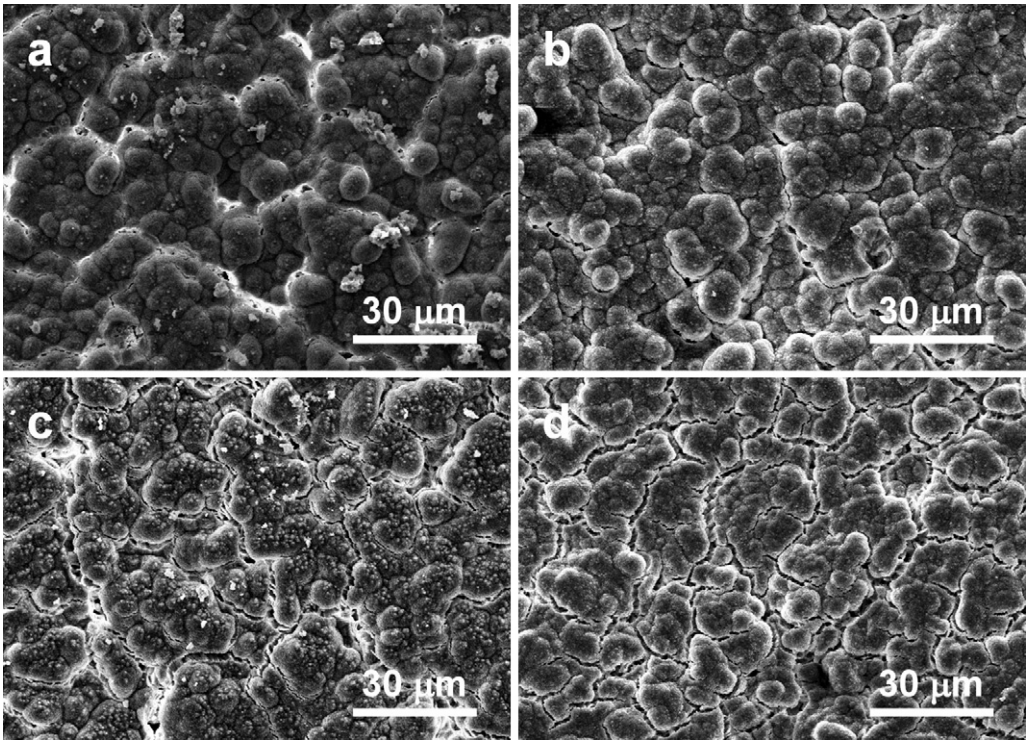


**Fig. 3.** Microstructure of EBD 10Sc1CeSZ electrolyte film after deposition and annealing: (a) deposition at 1173 K, annealing at 1473 K; (b) deposition at 873 K, annealing at 1178 K; (c) deposition at 1023 K, annealing at 1473 K; (d) deposition at 873 K, annealing at 1473 K.

**Table 1**
The effective elastic properties of 10Sc1CeSZ electrolyte film and thermal stresses corresponding to different $\Delta T$.

| $\Delta T$, K | $f_f$ | $E$, GPa | $\nu$ | $\sigma$, MPa |
|---|---|---|---|---|
| 150 | 0.039 | 194 | 0.30 | 60.6 |
| 300 | 0.392 | 147 | 0.23 | 85.6 |
| 305 | 0.473 | 138 | 0.21 | 80.6 |
| 375 | 1.358 | 69 | 0.11 | 45.0 |
| 450 | 2.103 | 38 | 0.06 | 28.9 |
| 460 | 2.414 | 30 | 0.05 | 23.0 |
| 600 | 3.365 | 14 | 0.02 | 13.9 |

decreasing effective thermal stresses in the electrolyte. The effective elastic properties of the electrolyte and acting thermal stresses corresponding to different $\Delta T$ are listed in Table 1. The dependence of the tensile stresses on microcrack density can be compared with the model calculations.

The results of statistical analysis of microcrack length (histograms and logarithmic normal distributions) for different $\Delta T$ of 300, 305, 375, 450, 460 and 600 K are shown in Fig. 4. The average microcrack size and the standard deviation which correspond to the temperature difference $\Delta T$ = 300 K are 11.79 and 5.56 μm, respectively (Fig. 4a); the number of microcracks revealed experimentally in the scanned area is 104. At a temperature difference $\Delta T$ = 305 K the average microcrack size and the standard deviation equal 12.6 and 7.54 μm, respectively (Fig. 4b); the corresponding number of microcracks is 99 in this case. The average microcrack size and the standard deviation corresponding to temperature difference $\Delta T$ = 375 K are 20.40 and 10.03 μm, respectively; the number of microcracks is 118. The average microcrack size and the standard deviation corresponding to temperature difference $\Delta T$ = 450 K are 26.53 and 10.95 μm, respectively (Fig. 4c); the number of microcracks is 115. At a temperature difference $\Delta T$ = 460 K the average microcrack size and the standard deviation equal 25.58 and 13.88 μm, respectively; the number of microcracks revealed is 128. At a temperature difference $\Delta T$ = 600 K the average microcrack size and the standard deviation equal 29.29 and 15.79 μm, respectively (Fig. 4d); the number of microcracks revealed is 137. The experimental data obtained indicate the fact that increasing $\Delta T$ brings about an insignificant growth of the number of microcracks which in fact can be considered as a constant value within the statistical scatter of data. At the same time, a marked growth of both the average microcrack size and the standard deviation are observed. For comparison, the appropriate logarithmic normal distributions of microcrack sizes along with the logarithmic normal distributions of grain sizes are shown in Fig. 5. It is seen that the distribution for microcrack sizes are wider compared to that for grain sizes. In addition, the distribution of microcrack sizes becomes wider with $\Delta T$ increasing.

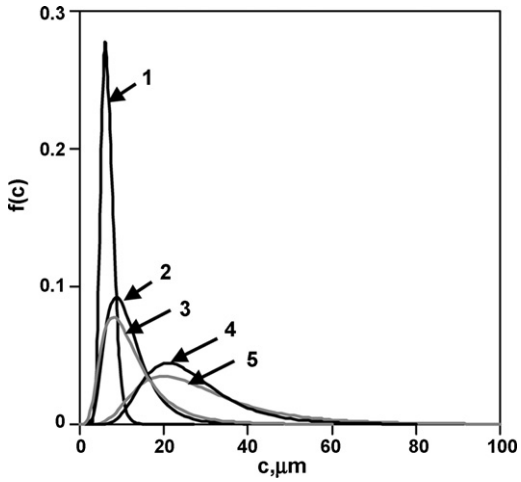


**Fig. 5.** Logarithmic normal distributions of grain sizes and crack sizes in the electrolyte film: 1—grain sizes; 2—crack sizes at temperature difference of 300 K; 3—crack sizes at temperature difference of 305 K; 4—crack sizes at temperature difference of 450 K; 5—crack sizes at temperature difference of 600 K.

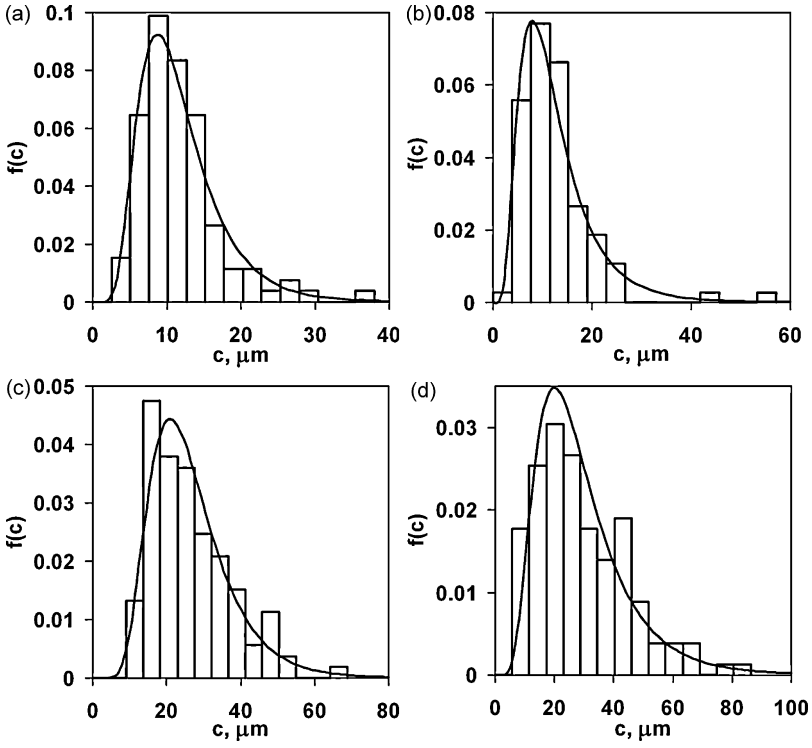


**Fig. 4.** Histograms and the corresponding logarithmic normal distributions of microcrack sizes in the electrolyte film after deposition and annealing: (a) deposition at 1173 K, annealing at 1473 K; (b) deposition at 873 K, annealing at 1178 K; (c) deposition at 1023 K, annealing at 1473 K; (d) deposition at 873 K, annealing at 1473 K.

It is important to note that the combination of experimental observations of microcrack density at different annealing temperatures with model calculations allows the critical parameters of electrolyte failure, such as maximum strain energy density $Q_c$ and strain energy density corresponding to microcracking initiation $q_0$, as well as the corresponding stresses to be determined.

As a rule, the calculation of microcracking parameters using (18) and (19) gives the dependencies of stress and strain energy density on microcrack density having maxima and the non-zero strain energy density corresponding to zero microcrack density. This means that a certain value of strain energy density $q_0$ is necessary for initiating microcracks. The normalised value of this parameter $q_0^*$ is given by expression (13), the corresponding stress value is:

$$\sigma_0 = \sqrt{2q_0E}. \tag{23}$$

The values of maximum stress and normalised maximum stress are designated as $\sigma_{\max}$ and $\sigma^*_{\max}$, respectively. The microcrack density corresponding to the maximum stress is less than that corresponding to the maximum strain energy density. After reaching maximum strain energy density the microcracking process develops catastrophically when fracture becomes localised and each next grain fails at the tip of the existing crack. In such a situation the total number of cracks remains practically constant. Eventually, the total failure of a material occurs in this stage of microcracking. Therefore, the maximum value of strain energy density $Q_c$ (the normalised value of this parameter is designated as $Q_c^*$ and given by (13)) can be used as a critical parameter corresponding to failure. Note that the proposed model which describes scattered microcracking allows the start point of localised microcracking to be determined.

In case of uniaxial tension, the critical stress $\sigma_c$ which corresponds to strain energy density $Q_c$ is as follows

$$\sigma_c = \sqrt{2Q_cE}. \tag{24}$$

Note that for brittle materials the uniaxial tension strength equals the equibiaxial tension strength [32]. This means that in the equibiaxial stress state the critical stress $\sigma_c$ can be set to be comparable with the thermal residual stress $\sigma_r$ in the electrolyte.

The parameter necessary for model calculations but unknown at this stage is the specific energy of new surface creation $\gamma$. An attempt is made here to determine this parameter for the electrolyte material analysing the experimental data from the point of view of some limitations imposed on microcracking parameters. First of all, the dependence of the average microcrack size $\langle c\rangle$ on the minimal size of failed element $l^*$ can be calculated using (20), i.e. based on the assumption of scattered microcracking. The results of this calculation are shown in Fig. 6a, curve 1. In this case all points of the curve $\langle c\rangle = f(l^*)$ have no dependence on $\gamma$. Next, each of the experimentally determined average microcrack sizes can be considered as being in correspondence with a given parameter $l^*$ which can be found from (19) prescribing some specific value to $\gamma$. The position of a point corresponding to maximum strain energy density (i.e. to localised microcracking initiation) depends on $\gamma$ too, but in fact this dependence is negligible. Note that all points of curve 1 to the left of the indicated point (which corresponds to localised microcracking initiation), are shown for comparison only and do not describe any real process. Because curve 1 demonstrates the decrease of parameter $\langle c\rangle$ upon decreasing $l^*$, but experimental points at the temperature difference $\geq$300 K for any value of $\gamma$ demonstrate opposite tendency, i.e. growth of the average microcrack size $\langle c\rangle$ upon $l^*$ decreasing, the conclusion can be made that annealing heat treatments caused the localised microcracking. Taking into account that, in line with the model assumptions, localised microcracking initiation corresponds to achieving maximum strain energy density $Q_c$, and a fracture is an irreversible process running with continuous decrease of $l^*$, it follows that all experimental points in Fig. 6a may not be located to the right of the point which corresponds to $Q_c$. First of all, this restriction concerns the experimental point with minimal average size of microcrack. Thus, it follows from (19) that, other conditions being equal, $\gamma$ cannot exceed a given value $\gamma_u$; in other words, we have a boundary for parameter $\gamma$: $\gamma < \gamma_u$.

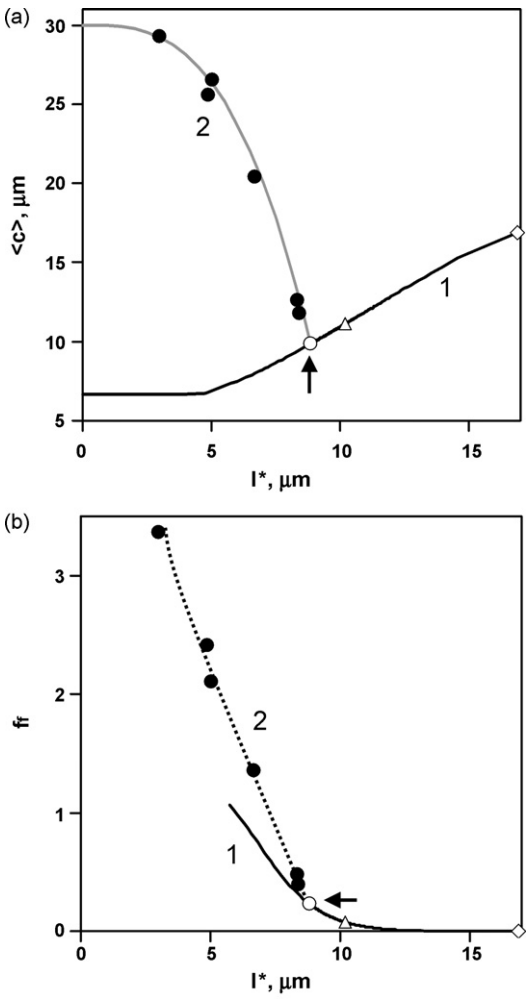


**Fig. 6.** Dependencies of the average crack size (a) and microcrack density (b) on minimal size of failed grain for electrolyte film 10Sc1CeSZ: 1—scattered microcracking; 2—localised microcracking; the arrow indicates the transition from scattered to localised microcracking; filled circles, open circle, triangle and rhomb designate experimental points, maximum strain energy density, maximum stress and microcracking initiation, respectively.

Shown in Fig. 6b is the dependence of the microcrack density $f_f$ on the parameter $l^*$ obtained using (18). It is seen that for a given $f_f$ value the points corresponding to localised microcracking (curve 2) are on the right of the points which correspond to scattered microcracking (curve 1). According to (19), other conditions being equal, the points for localised microcracking correspond to less stress as compared to points for scattered microcracking. Thus, the experimental points for localised microcracking must be located lower than curve 1 describing the dependence of stress on microcrack density for scattered microcracking (Fig. 7). Note that the decrease of the parameter $\gamma$ will shift points of curve 1 downwards. In other words, parameter $\gamma$ cannot be less than some given value $\gamma_l$, signifying the lower boundary, $\gamma > \gamma_l$. Based on the existence of the above two restrictions, in our case the lower boundary $\gamma_l$ and upper boundary $\gamma_u$ of parameter $\gamma$ were found to equal 0.035 and 0.037 J m$^{-2}$, respectively. This means the best estimation of

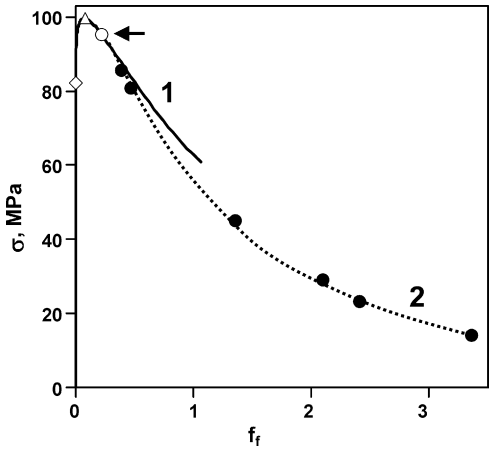


**Fig. 7.** Dependence of stress on microcrack density for a 10Sc1CeSZ electrolyte films: 1—scattered microcracking; 2—localised microcracking; the arrow indicates the transition from scattered to localised microcracking; filled circles, open circle, triangle and rhomb designate experimental points, maximum strain energy density, maximum stress and microcracking initiation, respectively.

the specific energy of new surface creation (with accuracy of 3%) is $\gamma = 0.036\,\mathrm{J\,m^{-2}}$.

The question arises to what measure the obtained value of the specific energy of new surface creation is realistic and how it compares with literature data. According to the authors' knowledge, the surface energy of 10Sc1CeSZ has not been determined to date. Experimental values of the surface energy of pure $ZrO_2$, according to different references, are as follows: $1.294\,\mathrm{J\,m^{-2}}$ (high-temperature wetting experiments with liquid metals) and $0.0559\,\mathrm{J\,m^{-2}}$ (low temperature wetting experiments with biological liquids) [33]; $6.5 \pm 0.2\,\mathrm{J/m^2}$ (monoclinic zirconia), $2.1 \pm 0.05\,\mathrm{J\,m^{-2}}$ (tetragonal zirconia), $0.5 \pm 0.05\,\mathrm{J\,m^{-2}}$ (amorphous zirconia) [34]—measured by oxide melt solution calorimetry; 0.77 and $1.13\,\mathrm{J\,m^{-2}}$ (tetragonal and monoclinic zirconia) [35]. For polycrystalline $ZrO_2$ containing 8% $Y_2O_3$, Tsoga and Nikolopoulos [36] extrapolated high-temperature data to get a surface energy of $1.927\,\mathrm{J\,m^{-2}}$ at 0 K. It is obvious that the value of the specific energy of new surface creation ($0.036\,\mathrm{J\,m^{-2}}$) for 10Sc1CeSZ electrolyte obtained in our work is reduced essentially in comparison with specific surface energy values of zirconia-based ceramics given in literature. The main reason of the reduction in our opinion can be attributed to the intercrystalline fracture mode of electrolyte film (Fig. 1). It is known that the energy of intergranular fracture of polycrystalline materials decreases to some extent compared to the energy of transcrystalline fracture. The decrease is widely considered to be associated with the occurrence of impurity atoms and their segregation to grain boundaries. The segregation is known to affect both mechanical properties and conductivity of ceramics [37–42]. In addition to this possible impurity effect, in our opinion, a second reason for the low specific energy of new surface creation of electrolyte film cannot be ruled out. This is associated with an intrinsic weakness of grain boundaries of the electrolyte film resulting from EBD processing and from its columnar structure. Considering above arguments, it is evident that the energy of free surfaces formed upon intercrystalline brittle failure should be used in our model calculations instead of the surface energy.

Taking the specified value of the specific energy of new surface creation as $0.036\,\mathrm{J\,m^{-2}}$, the dependence of the average microcrack size on the minimal size of failed grain $l^*$ was found to be described satisfactorily by the expression

$$\langle c \rangle = 30 - 0.029 l^{*3}, \tag{25}$$

where $\langle c \rangle$ and $l^*$ are in micrometers. Expression (25) indicates an existence of ultimate average microcrack size being 30 μm. Meanwhile, we take into account the fact that a microcracking process runs from large-sized to fine-sized grains to finish theoretically with zero-sized grains.

Taking the specified value of $\gamma$, elastic modulus of undamaged electrolyte of 200 GPa and experimental grain size distribution, the critical parameters of electrolyte microcracking were calculated using expressions (18) and (19). The strain energy density corresponding to microcracking initiation and maximum strain energy density were established to be $q_0 = 0.017$ MPa and $Q_c = 0.027$ MPa, respectively. The stress which corresponds to microcracking initiation, maximum stress and stress corresponding to localised microcracking initiation were found to be $\sigma_0 = 82$ MPa, $\sigma_{max} = 100$ MPa and $\sigma_c = 95$ MPa, respectively. The microcrack density corresponding to maximum stress and to localised microcracking initiation were found to equal $f_{max} = 0.077$ and $f_c = 0.226$, respectively.

Taking into account the above critical parameters and using the dependencies of elastic modulus and Poisson ratios on microcrack density (10), (11), the values for the temperature difference $\Delta T$ corresponding to microcracking initiation, the maximum stress and the maximum strain energy density were found. The temperature differences are 195, 257 and 283 K, respectively. The temperature differences used in this work were 150, 300, 305, 375, 450, 460, and 600 K. Therefore, it is evident that the temperature difference of 150 K has not caused any microcracking, while temperature differences of 300, 305, 375, 450, 460, and 600 K were more than 283 K, thus corresponding to localised microcracking. Note also that the experimental determination of microcrack density in the electrolyte in conditions being within the range from microcrack initiation to maximum stress is a complicated task due to the fact that the corresponding microcrack densities are not far from the so-called background value which is observed in practically non-cracked material. Thus, it is realistic for scattered microcracking to reveal the conditions after maximum stress, i.e., being within the range from maximum stress to maximum strain energy density. In our case this is the range of temperature difference from 257 to 283 K which is a narrow temperature interval of 26 K only. Accounting also for the occurrence of statistical deviations in the microstructure of the electrolyte film, it is a difficult task to fit the annealing conditions into the temperature range of distinct scattered microcracking.

The determination of parameter $\gamma$ was based on the model assumption that localised microcracking begins at the moment of achieving maximum strain energy density. Fig. 8 is the additional evidence in favor of this assumption. Fig. 8a shows the dependence of a number of cracks per one grain $n^*/n_g^*$ upon microcrack density. It is seen that experimental values $n^*/n_g^*$ for all microcrack densities are located near the line depicting the calculated number of cracks per one grain which correspond to the maximum strain energy density. Taking into account the statistical character of experimental values $n^*/n_g^*$, it is realistic to consider that in first approximation the number of cracks at the stage of localised microcracking remains constant. The validity of the model calculations is confirmed also by Fig. 8b where both theoretical (scattered microcracking) and experimental (localised microcracking) dependences of the average microcrack size on microcrack density are shown. It is seen that these dependencies seem to intersect in the point which correspond to maximum strain energy density. In addition, the conclusion can be made that the average microcrack size for localised microcracking increases upon growth of $f_f$, demonstrating the tendency for saturation.

The standard deviation $s$ of microcrack sizes increases while the average microcrack size $\langle c \rangle$ decreases in the stage of scattered microcracking (Fig. 9, curve 1). Development of the localised microcracking causes a further increase of standard deviation and growth of the average microcrack size (Fig. 9, curve 2). The experimen-

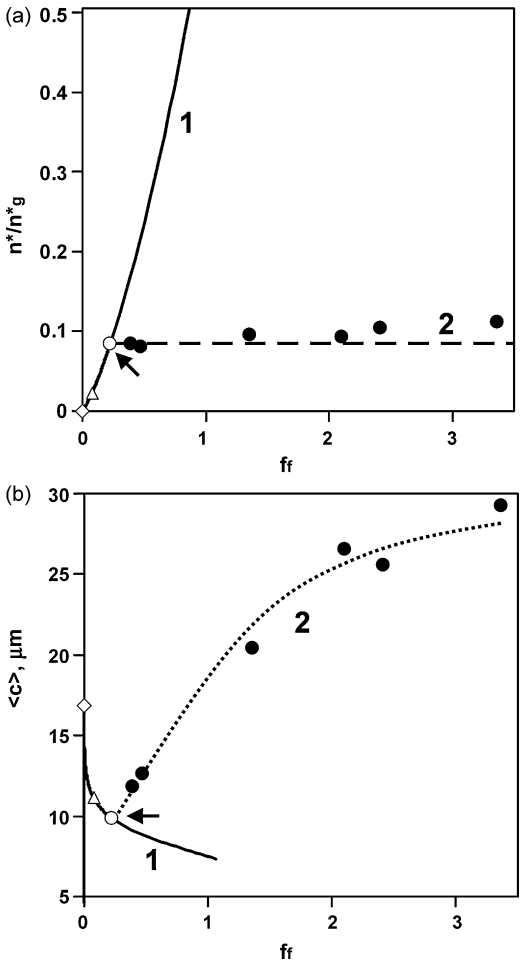


**Fig. 8.** Dependencies of the number of microcracks per one grain (a) and average microcrack size (b) on microcrack density for 10Sc1CeSZ electrolyte films: 1—scattered microcracking; 2—localised microcracking; the arrow indicates the transition from scattered to localised microcracking; filled circles, open circle, triangle and rhomb designate experimental points, maximum strain energy density, maximum stress and microcracking initiation, respectively.

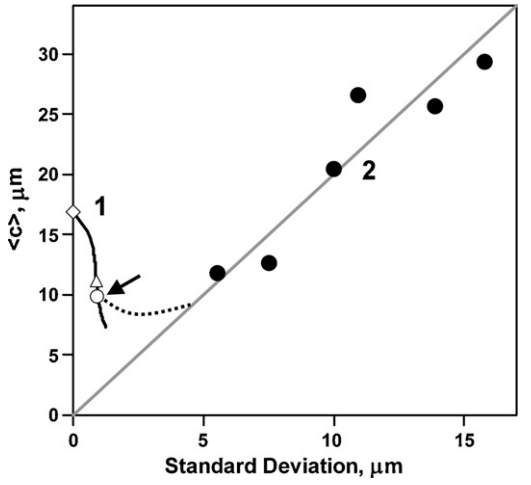


**Fig. 9.** Dependence of average microcrack size on its standard deviation for 10Sc1CeSZ electrolyte films: 1—scattered microcracking; 2—localised microcracking; the arrow indicates the transition from scattered to localised microcracking; filled circles, open circle, triangle and rhomb designate experimental points, maximum strain energy density, maximum stress and microcracking initiation, respectively.

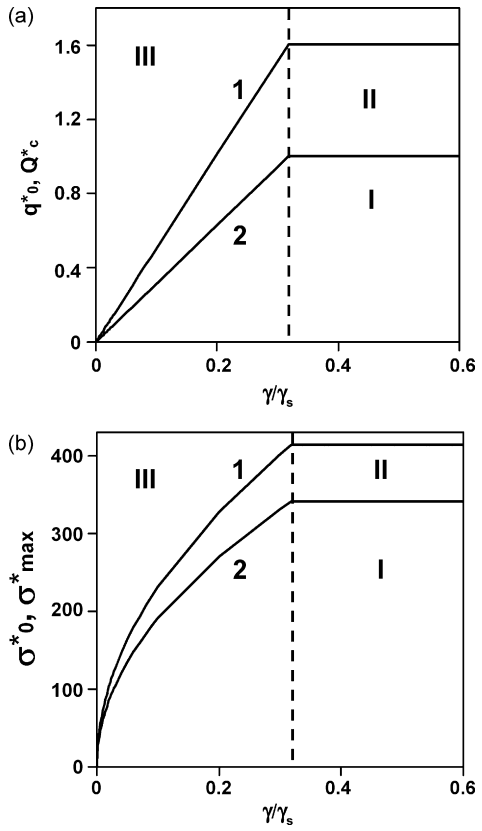


**Fig. 10.** Dependence of critical microcracking parameters on the parameter $\gamma/\gamma_s$ for 10Sc1CeSZ electrolyte films: (a) strain energy densities, (b) critical stresses; 1—maximum values; 2—values, corresponding to microcracking initiation; I—zone of undamaged material (below curve 2); II—zone of scattered microcracking (between curves 1 and 2); III—zone of localised microcracking (above curve 1); the dotted line is the boundary between transcrystalline and intercrystalline fracture.

tal dependence (i.e., localised microcracking) of $\langle c \rangle$ upon $s$ can be expressed in first approximation as $\langle c \rangle = 2s$.

It is of interest to know in what measure a variation of the parameter $\gamma$ will affect the critical parameters of the electrolyte film. The calculations were made taking the value of the true surface energy of the electrolyte film in first approximation to be $\gamma_s = 1.927\ \mathrm{J\,m^{-2}}$ [36]. The dependence of the normalised strain energy density on parameter $\gamma/\gamma_s$ for an electrolyte film of 10 μm in thickness is shown in Fig. 10. Curve 1 is the maximum strain energy density which corresponds to failure; curve 2 is the strain energy density which corresponds to microcracking initiation. There are three characteristic zones of the material behaviour. Zone I (below curve 2) is the zone of existence of undamaged material; zone II (between curves 1 and 2) and zone III (above curve 1) corresponds to scattered microcracking and catastrophic localised microcracking, respectively. Note that on the left of the dotted line the material will be susceptible to intercrystalline fracture. In this region the strain energy density is a linearly increasing function of the parameter $\gamma/\gamma_s$. On the right of the dotted line lies the range of transgranular failure where the strain energy density does not depend on $\gamma/\gamma_s$. According to the model assumptions, the critical value of $\gamma/\gamma_s$, corresponding to the transition from intercrystalline to transcrystalline fracture, is the ratio of the geometrical factors of the structural elements for transcrystalline cracks to that for intercrystalline cracks, which in the 2D case is 0.3183. The dependencies of stress corresponding to microcracking initiation (curve 2) and maximum stress (curve 1) on $\gamma/\gamma_s$ are shown in Fig. 10b. Similarly to Fig. 10a, three different zones can be found. The dotted line is the boundary between transcrystalline and intercrystalline frac-

ture. Within the zone of intercrystalline fracture the critical stresses increase with growth of the parameter $\gamma/\gamma_s$, but these dependencies are non-linear. Within the zone of transcrystalline fracture the critical stresses do not depend on $\gamma/\gamma_s$.

The second issue to be discussed is the effect of the electrolyte layer thickness on the microcracking process. It is obvious that the layer thickness will affect the microcracking density corresponding to saturation. The average distance between microcracks is limited by the layer thickness in having an effect on the saturation microcracking density. In our case, the minimum average distance between microcracks (for annealing with $\Delta T = 600$ K) is not less than 20 μm (a factor two higher than the layer thickness). Actually, we only observed a tendency to saturation but the saturation condition itself was not reached. In [43] the calculation procedure for critical stress (depending on layer thickness) to maintain tunnel crack growth was proposed. It was found that this is conservative: any flaw, regardless of its initial size or shape, cannot grow into a long tunnel if the applied stress is below the critical stress. Using the parameters of the 10Sc1CeSZ electrolyte the critical stress for crack tunneling was calculated to be 45 MPa which is less than the critical stresses calculated using the proposed model. This means that the occurrence of microcracking in the 10Sc1CeSZ electrolyte is also in accord with [43]. In addition, the proposed model takes the layer thickness indirectly into account. According to the model, all critical parameters of the microcracking process depend on the average grain size. However, in the 2D case considered in this work, the average grain size is comparable with the layer thickness.

## 5. Conclusions

The combination of electron microscopy data with model calculations permits both the specific energy of new surface creation of the electrolyte and critical parameters of the microcracking process to be determined. The best estimation of the specific energy of new surface creation (with an accuracy of 3%) is $\gamma = 0.036\ \mathrm{J\,m^{-2}}$. The strain energy density of microcracking initiation and maximal strain energy density are 0.017 and 0.027 MPa, respectively. The mechanical stress corresponding to microcracking initiation is 82 MPa; the maximum mechanical stress is 100 MPa; the mechanical stress corresponding to initiation of localised microcracking is 95 MPa. The microcrack densities which correspond to maximal stress and to the initiation of localised microcracking are 0.077 and 0.226, respectively.

The annealing-induced electrolyte microcracking described here corresponds to localised microcracking, when each next structural element fails mainly at existing microcrack tips. The following features of localised microcracking in EBM deposited 10Sc1CeSZ electrolyte are revealed: (i) the average microcrack size increases with microcrack density growth, demonstrating a tendency for saturation; (ii) the standard deviation of microcrack size is about half of the average microcrack size; (iii) the number of microcracks increases to a little degree; in first approximation it is a constant corresponding to a microcrack number at a moment when strain energy density is at a maximum. It is found also that the minimum value of average microcrack size is reached at a moment corresponding to maximum strain energy density.

However, it should be noted that the problem of electrolyte microcracking is far from a comprehensive understanding. Among the most prospective directions of future investigations the issues of further collection of experimental data as well as development of theoretical foundations of localised microcracking can be identified.

## Acknowledgements

The work was supported by INTAS Grant No. 06-1000024-8748 "Structure Optimization of SOFC Based on Scandia Doped Zirconia Ceramics for Space Application". We thank Dr. L. Dubykivskyy, Mr. Y. Brodnikovskyy and Mr. M. Brychevskyy from Institute for Problems of Materials Science, Kiev, Ukraine for half-cell fabrication and annealing, Dr. P. Batfalsky, Forschungszentrum Jüelich, Germany, for Scanning Electron Microscopy, Dr. J. Malzbender, Forschungszentrum Jüelich, Germany, for biaxial bending tests, Dr. R.W. Steinbrech, Forschungszentrum Juelich, Germany for helpful discussion.

## References

[1] D. Ghosh, Development of stationary solid oxide fuel cells, in: Proceedings Fuel Cell World (5th European SOFC Forum), Lucerne, 2002.
[2] S.C. Singhal, Solid oxide fuel cells for stationary, mobile, and military applications, Solid State Ionics 152–153 (2002) 405–410.
[3] N.Q. Minh, Ceramic fuel cells, J. Am. Ceram. Soc. 76 (1993) 563–588.
[4] R. Steinberger-Wilckens, J. Mergel, A. Glüsen, K. Wippermann, I.C. Vinke, P. Batfalsky, M.J. Smith, in: M. Gasik (Ed.), Materials for Fuel Cells, Woodhead Publishing, Cambridge, 2008, ISBN 1 84569 330 2.
[5] L. Blum, H.–P. Buchkremer, S.M. Gross, L.G.J. de Haart, J. Quadakkers, U. Reisgen, R. Steinberger-Wilckens, R.W. Steinbrech, F. Tietz, Overview of the development of solid oxide fuel cells at Forschungszentrum Juelich, Int. J. Appl. Ceram. Technol. 3 (2006) 470–476.
[6] J.M. Ralph, A.C. Schoeler, M. Krumpelt, Materials for lower temperature solid oxide fuel cells, J. Mater. Sci. 36 (2001) 1161–1172.
[7] S. Primdahl, B.F. Sorensen, M. Mogensen, Effect of nickel oxide/yttria-stabilized zirconia anode precursor sintering temperature on the properties of solid oxide fuel cells, J. Am. Ceram. Soc. 83 (2000) 489–494.
[8] C.M. Grgicak, R.G. Green, W.-F. Du, J.B. Giorgi, Synthesis and characterization of NiO–YSZ anode materials: precipitation, calcination, and the effects on sintering, J. Am. Ceram. Soc. 88 (2005) 3081–3087.
[9] J. Malzbender, E. Wessel, R.W. Steinbrech, Reduction and re-oxidation of anodes for solid oxide fuel cells, Solid State Ionics 176 (2005) 2201–2203.
[10] V. Sergo, D.M. Lipkin, G. de Portu, D.R. Clarke, Edge stresses in alumina/zirconia laminate, J. Am. Ceram. Soc. 80 (1997) 1633–1638.
[11] E. Maire, D.S. Wilkinson, J.D. Embury, R. Fougeres, Role of damage on the flow and fracture of particulate reinforced alloys and metal matrix composites, Acta Mater. 45 (1997) 5261–5274.
[12] C.-W. Nan, D.R. Clarke, The influence of particle size and particle fracture on the elastic/plastic deformation of metal matrix composites, Acta Mater. 44 (1996) 3801–3811.
[13] J.R. Brockenbrough, F.W. Zok, On the role of particle cracking in flow and fracture of metal matrix composites, Acta Metall. Mater. 43 (1995) 11–20.
[14] R. Estevez, E. Maire, P. Franciosi, D.S. Wilkinson, Effect of particle clustering on the strengthening versus damage rivalry in particulate reinforced elastic plastic materials: a 3-D analysis from a self-consistent modeling, Eur. J. Mech. A/Solids 18 (1999) 785–804.
[15] M. Lugovy, V. Slyunyayev, V. Teixeira, Residual stress relaxation processes in thermal barrier coatings under tension at high temperature, Surf. Coat. Technol. 184 (2004) 331–337.
[16] G. Gogotsi, M. Lugovy, Local stochastic analysis of microcracking and non-elastic behavior of ceramics, Theor. Appl. Fract. Mech. 36 (2001) 115–123.
[17] Y.N. Podrezov, N.I. Lugovoy, V.N. Slyunyaev, N.V. Minakov, Statistical failure model of materials with micro-inhomogeneity, Theor. Appl. Fract. Mech. 26 (1997) 35–40.
[18] M. Lugovy, N. Orlovskaya, K. Berroth, J. Kuebler, Microstructural engineering of ceramic-matrix layered composites: effect of grain-size dispersion on single-phase ceramic strength, Compos. Sci. Technol. 59 (1999) 283–289.
[19] S. Yarmolenko, J. Sankar, N. Bernier, M. Klimov, J. Kapat, N. Orlovskaya, Phase stability and sintering behavior of 10 mol% $Sc_2O_3$–1 mol%$CeO_2$–$ZrO_2$ ceramics, J. Fuel Cell Sci. Technol. 6 (2009) 021007.
[20] H. Kishimoto, N. Sakai, T. Horita, K. Yamaji, Y.-P. Xiong, M.E. Brito, H. Yokokawa, Rapid phase transformation of zirconia in the Ni-ScSZ cermet anode under reducing condition, Solid State Ionics 179 (2008) 2037–2041.
[21] N.I. Grechanyuk, V.A. Osokin, P.A. Shpak, E.L. Piyuk, Effect of production parameters on the structure of the outer ceramic layer in two-layer metal–ceramic coatings prepared by electron-beam deposition in one production cycle, Powder Metall. Met. Ceram. 44 (2005) 137–142.
[22] M. Lugovy, V. Slyunyayev, N. Orlovskaya, G. Blugan, J. Kuebler, M. Lewis, Apparent fracture toughness of $Si_3N_4$-based laminates with residual compressive or tensile stresses in surface layers, Acta Mater. 53 (2005) 289–296.
[23] M. Lugovy, V. Slyunyayev, V. Subbotin, N. Orlovskaya, G. Gogotsi, Crack arrest in $Si_3N_4$-based layered composites with residual stress, Compos. Sci. Technol. 64 (2004) 1947–1957.
[24] ASTM C 1499-05. Test Method for Monotonic Equibiaxial Flexural Strength of Advanced Ceramics at Ambient Temperature.
[25] R.W. Davidge, T.J. Green, The strength of two-phase ceramic/glass materials, J. Mater. Sci. 3 (1968) 629–634.
[26] B. Schultrich, Mechanical properties of brittle materials, in: Modern theories and experimental evidence. Akademie der Wissenschaften der DDR, Zentralinstitut fur Festkoerperphysik und Werkstofforschung, N32, 1986, s. 229–266.
[27] R.L. Salganik, Mechanics of solids with large number of cracks, Izv. AN SSSR (Mekhanika tverdogo tela) N4 (1973) 149–158 (in Russian).

[28] A. Karimi, Y. Wang, T. Cselle, M. Morstein, Fracture mechanisms in nanoscale layered hard thin films, Thin Solid Films 420–421 (2002) 275–280.
[29] V.T. Srikar, K.T. Turner, T.Y.A. Ie, S.M. Spearing, Structural design considerations for micro-machined solid-oxide fuel cells, J. Power Sources 125 (2004) 62–69.
[30] S. Giraud, J. Canel, Young's modulus of some SOFC materials as a function of temperature, J. Eur. Ceram. Soc. 28 (2008) 77–83.
[31] S.F. Corbin, X. Qiao, Development of solid oxide fuel cell anodes using metal-coated pore-forming agents, J. Am. Ceram. Soc. 86 (2003) 401–406.
[32] E. Hoek, Strength of jointed rock masses, in: 23rd Rankine Lecture. Geotechnique 33 (1983) 187–223.
[33] S. Agathopoulos, A.J. Calado, J.Y. Xu, M.C. Ferro, M.H.V. Fernandes, M. Nedea, P. Nikopoulos, R.N. Correia, Interactions at the surface of oxide bioceramics with biological liquids and blood cells, Key Eng. Mater. 240–242 (2003) 675–678.
[34] A. Navrotsky, Energetics of nanoparticle oxides: interplay between surface energy and polymorphism, Geochem. Trans. 4 (2003) 34–37.
[35] S. Zhao, K. Xu, The characterization of $ZrO_2$ films with different substrate bias voltages, J. Korean Phys. Soc. 46 (2005) S70–S74.
[36] A. Tsoga, P. Nikolopoulos, Surface and grain-boundary energies in yttria-stabilized zirconia (YSZ—8 mol%), J. Mater. Sci. 31 (1996) 5409–5413.
[37] S.(R.) Hui, J. Roller, S. Yick, X. Zhang, C. Deces-Petit, Y. Xie, R. Maric, D. Ghosh, A brief review of the ionic conductivity enhancement for selected oxide electrolytes, J. Power Sources 172 (2007) 493–502.
[38] S.P.S. Badwal, F.T. Ciacchi, K.M. Giampietro, Analysis of the conductivity of commercial easy sintering grade 3 mol% $Y_2O_3$–$ZrO_2$ materials, Solid State Ionics 176 (2005) 169–178.
[39] Y.-S. Jung, J.-H. Choi, J.-H. Lee, J.H. Lee, D.-Y. Kim, Impedance spectroscopic estimation of intergranular-phase distribution in $CaO{\cdot}2SiO_2$- or $SiO_2$-in-diffused 8 mol%-yttria-stabilized zirconia, Solid State Ionics 175 (2004) 123–127.
[40] F. Wakai, T. Nagano, T. Iga, Hardening in creep of alumina by zirconium segregation at the grain boundary, J. Am. Ceram. Soc. 80 (1997) 2361–2366.
[41] Y. Ikuhara, H. Yoshida, T. Sakuma, Impurity effects on grain boundary strength in structural ceramics, Mater. Sci. Eng. A 319–321 (2001) 24–30.
[42] J. Chevalier, C. Olagnon, G. Fantozzi, H. Gros, Creep behaviour of alumina, zirconia and zirconia-toughened alumina, J. Eur. Ceram. Soc. 17 (1997) 859–864.
[43] S. Ho, Z. Suo, Tunneling cracks in constrained layers, J. Appl. Mech. 60 (1993) 890–894.